nature climate change

Article

https://doi.org/10.1038/s41558-023-01599-3

More frequent atmospheric rivers slow the seasonal recovery of Arctic sea ice

Received: 21 February 2022

Accepted: 5 January 2023

Published online: 6 February 2023



Check for updates

Pengfei Zhang ®¹⊠, Gang Chen ®², Mingfang Ting ®³, L. Ruby Leung ®⁴, Bin Guan © 5,6 & Laifang Li^{1,7,8}

In recent decades, Arctic sea-ice coverage underwent a drastic decline in winter, when sea ice is expected to recover following the melting season. It is unclear to what extent atmospheric processes such as atmospheric rivers (ARs), intense corridors of moisture transport, contribute to this reduced recovery of sea ice. Here, using observations and climate model simulations, we find a robust frequency increase in ARs in early winter over the Barents-Kara Seas and the central Arctic for 1979-2021. The moisture carried by more frequent ARs has intensified surface downward longwave radiation and rainfall, caused stronger melting of thin, fragile ice cover and slowed the seasonal recovery of sea ice, accounting for 34% of the sea-ice cover decline in the Barents-Kara Seas and central Arctic. A series of model ensemble experiments suggests that, in addition to a uniform AR increase in response to anthropogenic warming, tropical Pacific variability also contributes to the observed Arctic AR changes.

Recent decades have witnessed a rapid decline in Arctic sea ice during its winter ice-growing season¹, which has raised concerns as Arctic sea-ice changes may fuel severe winter storms in mid-latitude continents²⁻⁴ and reshape the ecosystem and fisheries in the Arctic^{5,6}. Winter sea-ice area (SIA) decline, especially in the Barents-Kara Seas, has been attributed to poleward atmospheric moisture transport (for example, refs. ⁷⁻⁹), while enhanced oceanic heat transport through the Nordic Sea has aggravated ice thinning¹⁰⁻¹⁵.

The bulk of Arctic moisture import is driven by atmospheric rivers (ARs)¹⁶, which are long, narrow transient corridors of strong horizontal moisture transport, typically accompanied by a low-level jet ahead of an extratropical cyclone¹⁷. ARs account for up to 90% of the poleward water vapour transport in mid-latitudes^{18,19}, playing a crucial role in the hydrological cycle (for example, refs. ^{20,21}). As ARs can extend into the Arctic circle²², there is a need to quantify the role of ARs in ongoing Arctic climate change.

In polar regions, contrary to AR-induced snow accumulation in East Antarctica²³, the intense moisture and heat that are rapidly transported by ARs can exert a strong melting effect on the cryosphere. exemplified by ice sheet melt in Greenland²⁴ and West Antarctica²⁵, polynyas in the Weddell Sea²⁶ and the 2016–2017 record low Arctic winter sea-ice growth²². The physical processes relevant to AR-induced ice melt or impeded ice growth include (1) enhanced downward longwave radiation (DLW) due to the greenhouse effect of water vapour, the cloud radiative effect (CRE) and condensational heating release, (2) reduction or even sign change in turbulent heat fluxes from the ice surface, (3) the insulating capacity of snow and (4) melt energy carried by rainfall (for example, refs. 22,25-31).

In recent decades, more frequent ARs have been observed in Greenland and West Antarctica 24,25 , coinciding with the poleward shift of ARs in a warming climate $^{32-34}$. This study reports an increased AR frequency over the sea-ice-covered Eurasian Arctic. Given the melting effect of ARs, we hypothesize that more frequent Arctic ARs contribute to winter sea-ice decline. Although previous works have reported some AR-like plumes, such as meridional moisture intrusions that can induce cold-season sea-ice loss^{8,35}, these synoptic systems only account for

Department of Meteorology and Atmospheric Science, The Pennsylvania State University, University Park, PA, USA. Department of Atmospheric and Oceanic Sciences, University of California Los Angeles, Los Angeles, CA, USA. 3Lamont-Doherty Earth Observatory, Columbia University, Palisades, NY, USA. ⁴Atmospheric Sciences and Global Change Division, Pacific Northwest National Laboratory, Richland, WA, USA. ⁵Joint Institute for Regional Earth System Science and Engineering, University of California Los Angeles, Los Angeles, CA, USA. 6 Jet Propulsion Laboratory, California Institute of Technology, Pasadena, CA, USA. ⁷Earth and Environmental Systems Institute, The Pennsylvania State Univeristy, University Park, PA, USA. ⁸Institute for Computational and Data Sciences, The Pennsylvania State University, University Park, PA, USA. Se-mail: pfz5053@psu.edu; zpengfei1006@gmail.com

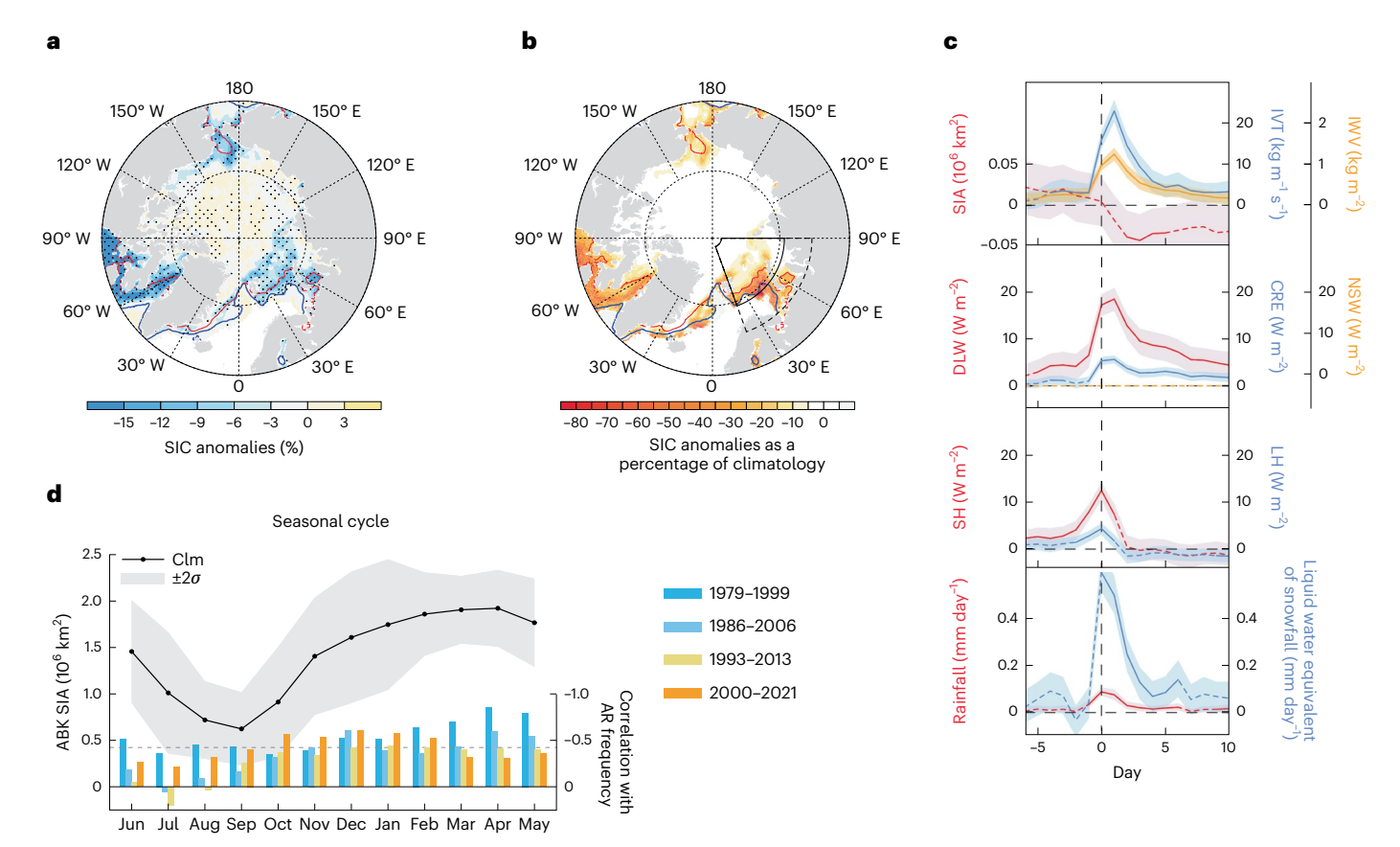


Fig. 1 | **Relationship between ARs and Arctic sea ice. a**, NSIDC SIC anomalies associated with ARs in NDJ for 1979–2021 (Methods). Red and blue lines are the climatological ice edges on 31 October and 31 January, respectively. Dots denote anomalies that are statistically significant at the 0.05 level according to 1,000 bootstrap samples. **b**, Same as **a** but for the SIC anomalies as a percentage of the climatology. The black outline (74–88° N, 20–90° E) highlights the ABK region. **c**, Composite temporal evolution of the anomalies of the selected variables in the ABK when ARs make landfall on the ice edge. IWV, vertical integral of water vapour; IVT, vertical integral of horizontal water vapour transport; LH, surface latent heat flux; NSW, net shortwave radiation; SH, surface sensible heat flux. SIA is the total ice area in the ABK calculated using NSIDC SIC (Methods), while other variables are area-averaged from ERA5 reanalysis. Day 0 is the day of AR 'landfalling' (defined as at least one grid

cell of an AR reaching the ice edge in the ABK). The solid segments denote the significant anomalies at 0.05 level while the colour shading denotes the 2.5–97.5% intervals based on 1,000 bootstrap samples. **d**, Seasonal cycle of SIA over the ABK region and its correlation with AR frequency. Given that the ice cover around ABK in late winter may extend to the coast, we extend the southern boundary of the ABK to 68° N (the dashed outline in **b**) for the SIA calculation. The black line is the climatology for 1979–2021 with an interval of 2σ (grey shading). The bars are the correlation coefficients between AR frequency and SIA in four overlapping 21-yr segments for 1979–2021 (right *y*-axis, note the inverted scale). A three-month running average is applied before the correlation calculation; the bars in Dec indicate the NDJ values. The correlation of bars extending above the dashed line is significant at the 0.05 level.

a small portion $(36-38\%)^8$ of Arctic moisture import compared with ARs $(70-80\%)^{16}$ (Supplementary Text 3). Furthermore, it is unclear to what extent human activities have contributed to the high-latitude AR changes in the past few decades, affecting mitigation and adaptation planning related to the rapidly changing Arctic water cycle.

This study examines the changes in Arctic ARs and their role in slowing down winter Arctic sea-ice recovery. The tropical Pacific features the most prominent modes of natural climate variability and exerts a stronger influence on the Arctic than any other ocean basin ^{36–38}, so we utilize a pacemaker approach with a state-of-the-art climate model to quantify the contributions of anthropogenic forcing and the observed sea surface temperature (SST) variability over the tropical Pacific to Arctic AR changes. We also clarify the mechanisms behind the Arctic AR changes by separating the dynamic (circulation change) and thermodynamic (moistening trend) effects. By focusing on ARs, we connect Arctic sea-ice changes with phenomenologically understood extreme weather events (ARs) that account for a large portion of Arctic moisture import.

The melting effect of ARs on Arctic sea ice

The melting effect of Arctic ARs during the ice recovery season (November–December–January (NDJ)) for the period 1979–2021 (Methods)

is shown in Fig. 1. The negative sea-ice concentration (SIC) anomalies associated with ARs indicate that they significantly slow ice growth throughout all marginal seas, including the Barents–Kara Seas, the Labrador Sea, Baffin Bay and the Chukchi–Bering Seas (Fig. 1a). In the Atlantic sector where the newly formed ice cover is thin 10,11 , ARs cause up to 60% of the sea-ice melting (Fig. 1b), resulting in a reduction of $\sim\!5\times10^4$ km² SIA (Methods) in the Barents–Kara Seas and the neighbouring central Arctic (ABK, outlined in Fig. 1b) within 3–4 days (Fig. 1c). This AR-driven sea-ice retreat is supported by the results from a pre-industrial simulation without background warming (Extended Data Fig. 1).

The melting effect of ARs on sea ice is dominated by extensive DLW (partly contributed by clouds within ARs) from the water vapour carried by ARs, as well as AR-induced rainfall (Fig. 1c). The snowfall associated with ARs could cause an insulating effect at the sea-ice surface that inhibits ice growth over a much longer timescale (throughout the winter) in this region³⁰, while anomalies in surface turbulent fluxes rapidly decay after the AR landfall. The AR occurrence is significantly correlated with negative ABK SIA anomalies during the ice recovery season, which is robust for 1979–2021 (Fig. 1d).

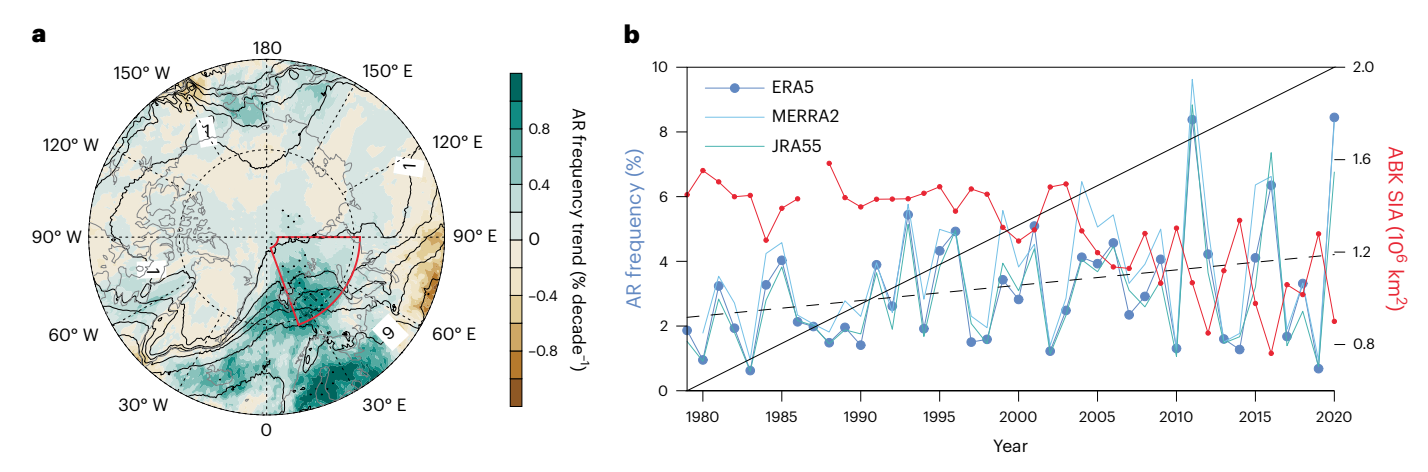


Fig. 2 | **Arctic AR frequency trends in NDJ for 1979–2021. a**, AR frequency trends from the ERA5 reanalysis. Contours are climatology. Dots denote trends that are statistically significant at the 0.05 level according to Student's *t*-test. **b**, Area-averaged AR frequency time series in the ABK area (highlighted by the red outline in **a**) from three reanalysis datasets (European Centre for Medium-Range Weather Forecasts 5th generation reanalysis (ERA5); Modern-Era Retrospective analysis

for Research and Applications, version 2 (MERRA2); and Japan Meteorological Agency Japanese 55-year Reanalysis (JRA55)). The dashed grey line is the linear trend of the ensemble mean of the three datasets. The red line is the time series of area sum SIA in the ABK with missing data in NDJ for 1987–1988. Both the AR and SIA trends (0.47% decades $^{-1}$ and -0.13×10^6 km 2 decade $^{-1}$) are significant at the 0.05 level based on Student's t-test.

Increased AR penetration into the Arctic and sea-ice impacts

In the past few decades, the Arctic has seen a significant increase in AR frequency in the early winter over ABK. This AR trend is robust across three observational datasets (Fig. 2b and Supplementary Fig. 1b,c), coinciding with the most pronounced winter sea-ice decline in this region (for example, ref. 39). In contrast, fewer ARs reach inland Eurasia (60–90° E) to the south of ABK.

Considering the strong melting effect of ARs, it is important to determine whether more frequent ARs could have contributed to the sea-ice decline in recent decades. The observed early winter SIC trend for 1979–2021 features a pronounced decline in the marginal seas, including the ABK, the Greenland Sea, the Labrador Sea and the Chukchi Sea (Supplementary Fig. 4a), where ARs exert the melting effect (Fig. 1). Since the melting effect of ARs on the shrinkage of Arctic sea-ice cover is manifested by DLW and rainfall (Fig. 1c), we show the trends of cumulated DLW and rainfall associated with ARs in NDJ in Fig. 3a,b. As the frequency of Arctic ARs increases in the ABK, the cumulated AR DLW is significantly intensified (Fig. 3a), which is partly due to the enhanced CRE (Extended Data Fig. 2a). The proportional contribution of the CRE to the cumulated AR DLW underscores the role of clouds in enhancing the AR-related DLW (Extended Data Fig. 3).

The cumulated AR rainfall, especially along the ice edge where the newice forms, is greatly strengthened (Fig. 3b), while the AR-induced snowfall changes are relatively small (Extended Data Fig. 2b). Although the heat carried by rainfall is minor^{28,40,41}, the higher correlation between SIC and rainfall with trends (-0.61) in the marginal ice zone of ABK compared with DLW (-0.47) during ARs suggests an increasing contribution of AR rainfall to sea-ice retreat. Quantifying the amount of energy input attributable to rainfall in comparison to other sources is outside the scope of this study and deserves further research. We also examined the above physical processes associated with the melting effect of ARs in the coupled climate model experiment of PAC2 (see 'Model experiments and interpretations' in Methods, which are analysed in the next section) in Fig. 3c,d and Extended Data Fig. 2c. The AR-induced DLW and rainfall significantly increase in the ABK, consistent with observations. These results suggest that the increased AR frequency could have enhanced the melting effect of ARs.

To quantify the role of ARs in sea-ice change, we examine the SIA growth in the ABK, defined as the cumulative sum of the daily anomalies

of SIA tendency in NDJ, with and without AR occurrences (Methods) (Fig. 4). Since the Arctic winter surface temperature in the current climate is below the freezing point despite the warming trend, it is expected that the general decline of sea ice in summer could lead to a faster thermodynamic ice growth in winter. Meanwhile, the ice has thinned due to oceanic warming¹²⁻¹⁵, and thinner ice grows faster^{10,11}. $Indeed, significantly faster SIA\,growth\,in\,NDJ\,is\,seen\,without\,the\,impact$ of the ARs (blue line in Fig. 4). Along with AR frequency increase, the melting effect on thin, fragile ice cover is enhanced (red line in Fig. 4), which partly offsets the fast thermodynamic SIA growth and results in a weak, non-significant positive trend in total SIA growth (black line in Fig. 4). Thus, frequent ARs can prevent the sea ice from growing to the extent allowed by the freezing temperature. On the basis of the melting effect of ARs on ABK SIA (red line in Fig. 4), we calculate the ABK SIA reduction associated with 1% AR frequency, which on average is $-8.8 \pm 0.6 \times 10^4$ km² in NDI (Methods). Then, by projecting the SIA reduction corresponding to 1% AR frequency to the actual AR frequency trend, we estimate the enhancement of the melting effect due to AR frequency increase, which accounts for ~34 \pm 2% of the total SIA decline in NDJ (Fig. 2b). Qualitatively similar results are found in the PAC2 simulations (dashed lines in Fig. 4). The SIA growth with and without ARs clearly demonstrates that more frequent ARs slow the seasonal sea-ice growth and therefore contribute to the SIA decline during the ice-growing season.

Drivers of Arctic AR frequency trends

To examine the causes of the Arctic AR trends, we first analysed the Global Ocean Global Atmosphere (GOGA2) experiment, an atmosphere-only model ensemble using CAM6/CESM2 forced by historical SST/SIC and radiative forcing that includes both the anthropogenic forcing and observed natural variability. Despite the bias of excessive ARs in the Bering Sea, the increasing ARs in the ABK, the AR climatology and the land–sea contrast of the AR changes in the Eurasian sector are closely reproduced in GOGA2 (Fig. 5a), suggesting that the model is capable of capturing the observed AR changes.

To identify the contribution of anthropogenic warming, we analyse the CESM2 Large Ensemble (LENS2), a coupled ocean–atmosphere–sea ice model forced by historical radiative forcing (Methods). The LENS2 ensemble mean, which corresponds to the model response to external radiative forcing, shows a uniform positive trend in AR frequency over

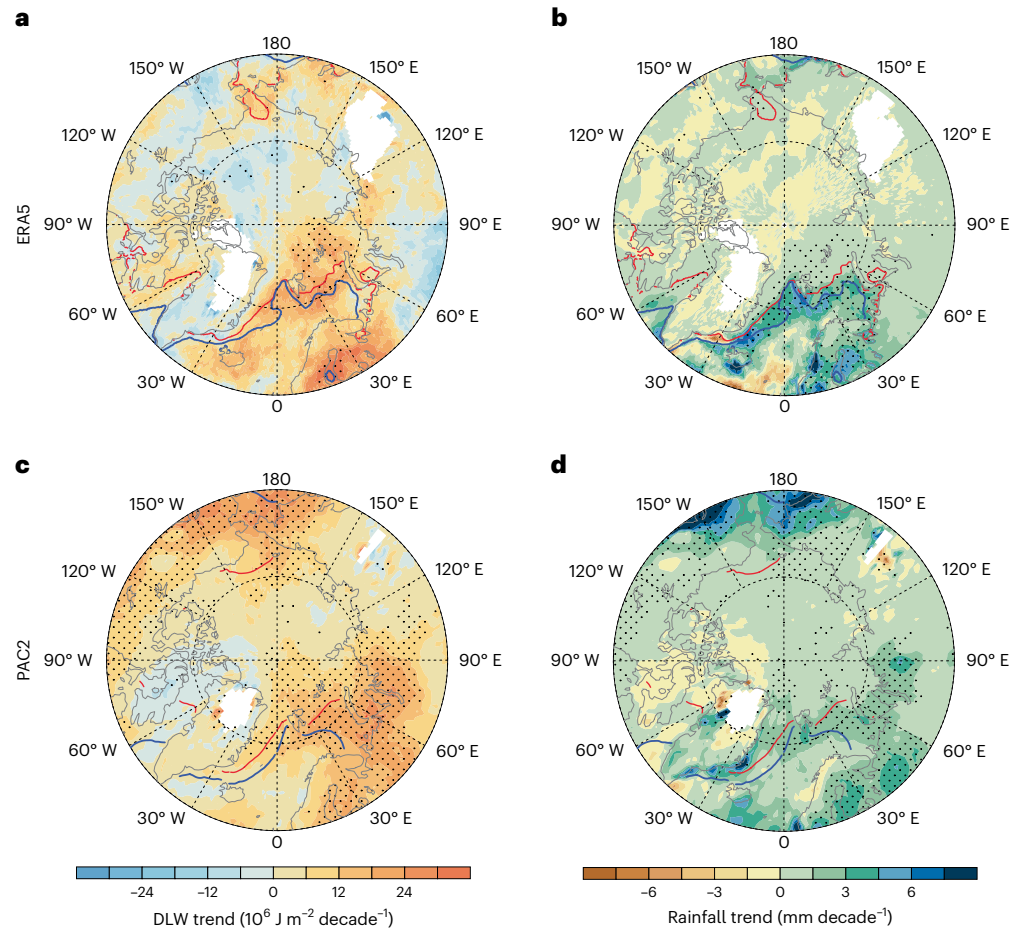
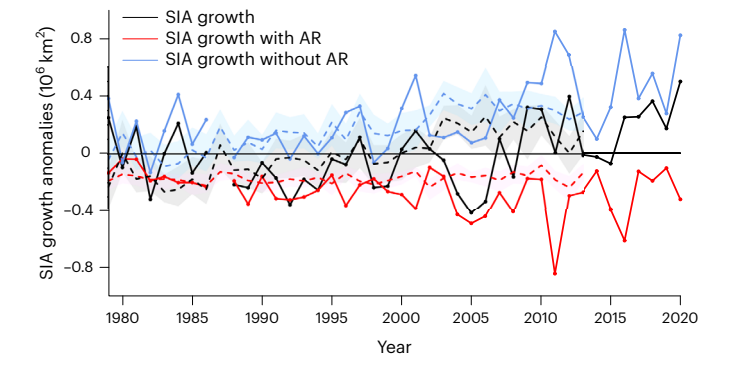


Fig. 3 | **Trends in the physical processes related to the AR melting effect in recent decades. a,b**, Linear trends in cumulated DLW (**a**) and rainfall (**b**) associated with ARs in NDJ in ERA5. See the calculation in Methods. The AR-induced total DLW in ERA5 can be validated by CERES-SYN satellite observations after 2000 (Supplementary Fig. 2). **c,d**, The same as **a,b** but for the model

ensemble from PAC2. Dots denote trends that are statistically significant at the 0.05 level according to Student's t-test for ERA5 and the 1,000 bootstrap samples for PAC2. Red and blue lines in $\mathbf{a} - \mathbf{d}$ are the climatological sea-ice cover edges on 31 October and 31 January, respectively, indicating the mean sea-ice growth in NDJ.

the entire high-latitude region (Fig. 5b). The maximum AR increase in LENS2 is in inland Eurasia, in contrast to fewer ARs in observations and GOGA2 for this region (Fig. 2a and Fig. 5a,b). Note that LENS2 and GOGA2 use the same atmosphere model and radiative forcing, except that GOGA2 is forced by observed variability in SSTs while LENS2 has internally generated SST variations with suppressed internal variability in its ensemble mean. The distinct spatial patterns of AR trends between LENS2 and GOGA2 suggest a possible role of the different SST variations. Although the model SST biases might contribute to the disagreement between the LENS2 ensemble mean and the observed or GOGA2 AR trends, some LENS2 members share high similarity with GOGA2 and are distinct from the ensemble mean (Extended Data Fig. 4). This further supports a possible role of internal variability in the modelled and observed AR trends.

To examine the contribution of the observed SST variability, we employ a pacemaker experiment (PAC2) that is the same as LENS2, except that the tropical Pacific SST anomalies (SSTa) are nudged towards the observed variations (Methods). We focus on the tropical Pacific here as it has the most prominent modes of natural climate variability, and it can exert a stronger influence on the Arctic than any other ocean basins ^{37,38}. Figure 5c shows that PAC2 captures the significant AR increases around the ABK region. With the tropical Pacific SST variability being the only difference between PAC2 and LENS2, the negative pattern correlation of the AR trend in LENS2 with 5th generation reanalysis (ERAS) (-0.39) in (0-120° E, 45-90° N) compared with



 $\label{eq:Fig.4} \textbf{ISIA growth in early winter.} \textbf{SIA growth is the cumulative sum of the daily anomalies of SIA tendency ((SIA;-1SIA;-)/2, where \textit{i} denote a day during 1 November to 31 January) in NDJ (Methods). The solid lines denote the total SIA growth for the whole season, SIA growth associated with the ARs and SIA growth without the effects of ARs from observations. The SIA growth associated with ARs denotes the melting effect of ARs on ABK SIA in NDJ. The negative trends in the melting effect and the positive trend in SIA growth without the impact of ARs are significant at the 0.05 level based on Student's t-test, while the trend in whole-season SIA growth is less significant. Similarly, the dashed lines show the ensemble mean SIA growth during the whole season, SIA growth associated with ARs and without the effects of ARs in PAC2 with corresponding standard errors (colour shading). The trend in the melting effect in PAC2 is less significant, although PAC2 closely reproduces the observed AR frequency change (Fig. 5). This may be attributable to the model bias in CESM2 sea-ice simulations (Methods).$

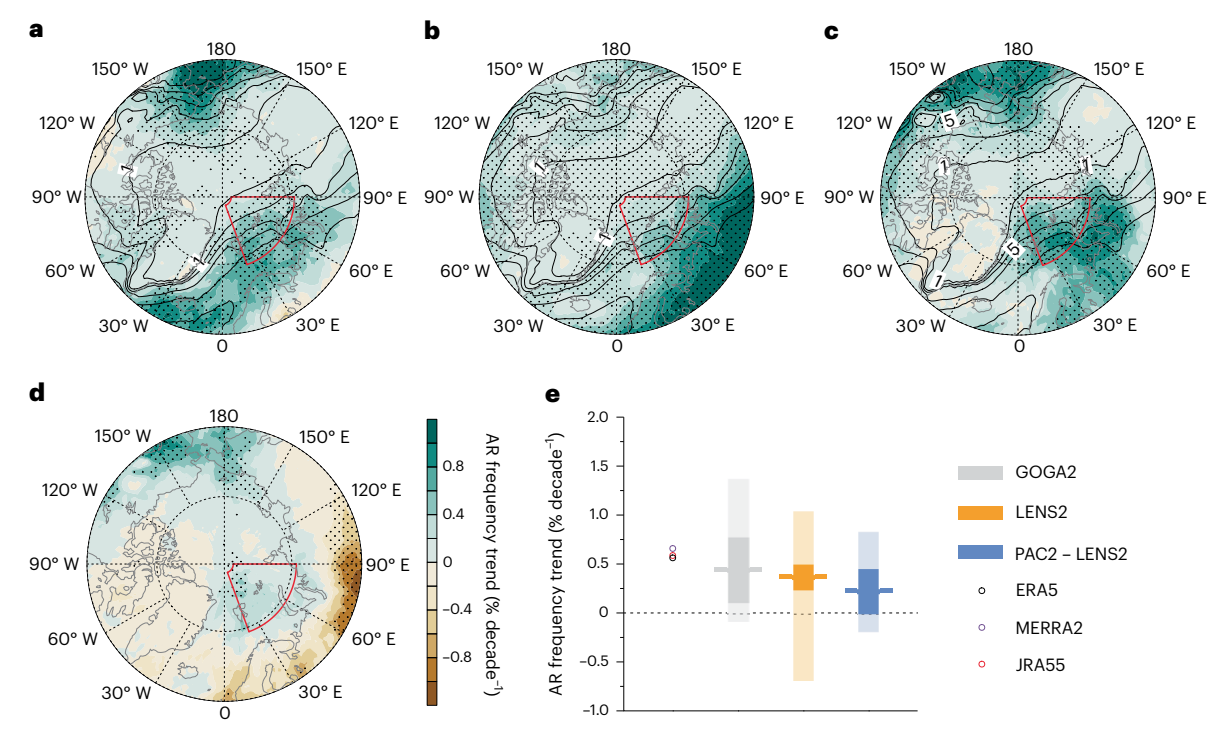


Fig. 5 | **AR frequency trends in NDJ in model ensembles. a–c,** Same as Fig. 2a but for the GOGA2 (a), LENS2 (b) and PAC2 (c) ensembles. Contours are corresponding climatology. Agreements in the sign of AR changes among members of each ensemble are shown in Supplementary Fig. 5. **d**, AR changes due to tropical Pacific variability calculated as the difference between the ensemble means of PAC2 and LENS2 (see 'Model experiments and interpretation' in Methods). Dots denote trends that are statistically significant at the 0.05 level according to 1,000 bootstrap samples in **a–d**, which is consistent with Student's *t*-test (Supplementary Fig. 5). **e**, Uncertainties in area-averaged AR trends in ABK (red outlines in **a–d**) in each model ensemble. The horizontal lines in the middle

of the bars represent the ensemble mean trends. The vertical solid bars show the 95% confidence interval of the ensemble mean following ref. 52 (Methods). The light vertical bars denote the 5th and 95th percentiles of the trends across the ensemble (that is, the minimum and maximum for GOGA2 and PAC2, 3rd minimum and maximum for LENS2). The blue bar is calculated on the basis of the ten members in PAC2 by removing the ensemble mean of LENS2, denoting the uncertainty of the contribution of tropical Pacific variability. The open circles show the trends in three reanalyses for 1979–2014 (the same period as model ensembles), representing the observation. Trends in three reanalyses are significant at the 0.05 level according to Student's t-test.

the positive correlation (0.44) in PAC2 suggests that the tropical Pacific influence is non-negligible and must be considered to fully understand the observed AR trends in the Arctic.

The PAC2 results are designed to represent the combined effects of anthropogenic warming and, at least partly, the observed tropical Pacific influence. Since these two factors are largely additive, the contribution of tropical Pacific variability can be obtained by calculating the differences between PAC2 and LENS2, as shown in Fig. 5d (see Methods for detailed interpretation and caveats). The observed variability from the tropical Pacific increases the AR frequency in the eastern Arctic, especially north of the ABK region, while significantly fewer ARs are found in inland Eurasia (Fig. 5d). These results suggest that tropical Pacific variability is crucial to the observed spatial pattern of AR changes around the Eurasian Arctic.

To further quantify the relative contributions of anthropogenic warming versus tropical Pacific influence, Fig. 5e shows the uncertainties of the area-averaged AR trends for ABK in the three sets of model experiments. The 95% confidence interval of the ensemble mean in GOGA2 encompasses the observed trend, indicating that the model forced with anthropogenic forcing and historical SST can capture the observed AR trend. In contrast, the observed AR trend is outside the 95% confidence interval of the anthropogenic change alone (LENS2) or the tropical Pacific influence alone (PAC2 – LENS2). This suggests that the observed AR change cannot be fully explained by either external forcing or tropical Pacific variability alone, but instead reflects the combined effect of anthropogenic forcing and internal climate variability. Based on Fig. 5e, the tropical Pacific influence accounts for $38 \pm 12\%$ of the

AR changes in PAC2. Note that the fraction will depend on the model's equilibrium climate sensitivity, which, at 5.3 K in CESM2, is larger than the best-estimated range of 1.5-4.5 K (ref. 42). It implies that the contribution of tropical Pacific SST variability could be even higher in reality.

Mechanisms of Arctic AR changes

We examined the mechanisms of the AR trends over the high latitudes, 0-110° E. Since water vapour transport is the product of wind and moisture content, the mechanisms of the AR changes in a warming climate can be roughly partitioned between the trends in wind (dynamic effect) and atmospheric moisture (thermodynamic effect) (for example, ref. ³⁴). The decomposition (Methods) is shown in Fig. 6. In observations, the AR increase in the ABK is dominated by the thermodynamic effect, while the lower number of ARs in west Eurasia is explained by the dynamic effect (Fig. 6a-c). The thermodynamic AR increases in the Arctic are consistent with the increase in the atmosphere's water holding capacity due to fast Arctic warming, which supports increased AR frequency observed in the Arctic in recent decades. The dynamical AR decrease in west Eurasia may be related to more persistent Ural blocking in recent decades⁴³, which suppresses cyclonic AR circulation. These land-sea contrasts in AR changes can also be seen in GOGA2 and PAC2, both partly constrained by the observed tropical Pacific variability (Fig. 6d-f,j-l). In fact, the tropical Pacific SSTa nudged to observations in the otherwise free-running PAC2 experiment can produce a tropical Pacific-Arctic teleconnection (for example, ref. 44), contributing thermodynamically to a warming Arctic through radiative feedback³⁶. This warming, induced by tropical Pacific variability in combination

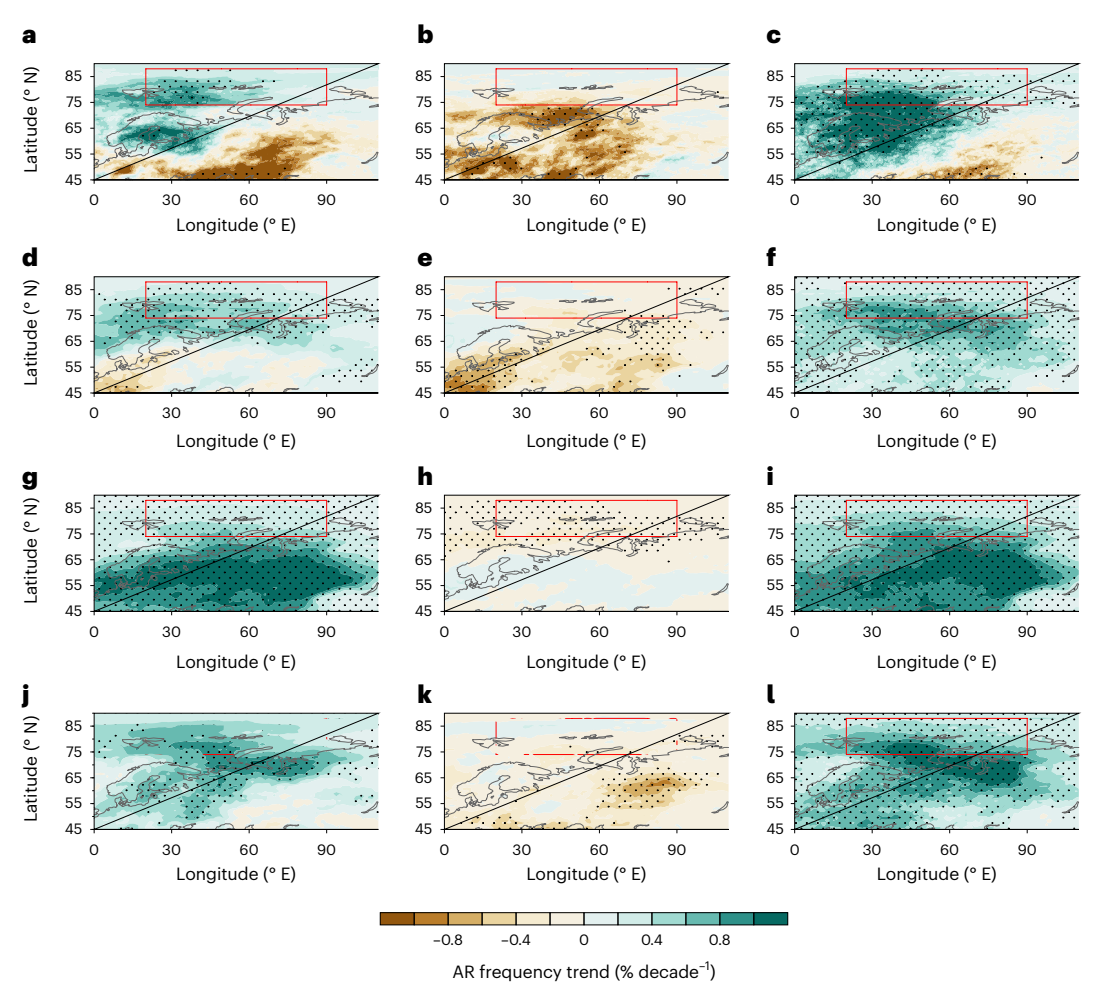


Fig. 6 | **Mechanisms of AR changes. a**, NDJ AR frequency trend in ERAS, which is reproduced from Fig. 2a but shown in cylindrical map projection here. **b**, **c**, Contributions of dynamic (**b**) and thermodynamic (**c**) effects to the AR trend in ERAS. **d**-**I**, Corresponding maps for GOGA2 (**d**-**f**), LENS2 (**g**-**i**) and PAC2 (**j**-**l**).

 $\label{eq:def} \textbf{d}, \textbf{g} \ \text{and} \ \textbf{j} \ \text{are reproduced from Fig. 5a-c} \ \text{but shown in cylindrical map projection}.$ Dots denote that the variables are statistically significant at the 0.05 level according to Student's \$t\$-test for \$\textbf{a}-\textbf{c}\$ and 1,000 bootstrap samples for \$\textbf{d}-\textbf{l}\$. The red box in each subplot delineates the ABK region.

with anthropogenic forcing, favours more frequent ARs in the Arctic, which is well captured by GOGA2 and PAC2 (Fig. 6f,l).

In contrast, there is a weak dynamical contribution and a strong thermodynamic increase in inland west Eurasia in the ensemble mean of LENS2 (Fig. 6h,i), leading to the maximum AR increase over west Eurasia (Fig. 6g and Fig. 5b). These differences between the LENS2 ensemble mean and observation in the spatial distributions of dynamic and thermodynamic effects can be attributed to the suppressed natural variability. Several ensemble members of LENS2, however, capture the maximum thermodynamic effect in the Arctic as in GOGA2 and PAC2 (Extended Data Fig. 4), further suggesting the important role of internal variability.

Conclusions

In this study, we show a robust frequency increase in ARs that penetrate into the Arctic in the ice-growing season for 1979–2021, especially over the ABK. ARs, which dominate the Arctic moisture import, induce a strong melting effect, especially on the newly formed thin and fragile sea ice, through enhanced DLW from the AR-transported water vapour and the associated rainfall. Given the thinner ice cover aggravated by warmer ocean water mass (for example, refs. $^{10,12-15}$), more frequent ARs result in a stronger melting effect on sea ice in ice-growing season, slowing down the seasonal sea-ice recovery in recent decades and accounting for 34 \pm 2% of the observed SIA decline in early winter in the ABK. Using state-of-the-art model

ensembles and a pacemaker experiment, we further demonstrate that, in addition to a uniform AR increase in response to anthropogenic forcing, the observed tropical Pacific SST variability is another vital driving factor of the observed AR changes around the Arctic in the past four decades. The increased frequency of Arctic ARs, in turn, is mainly driven by thermodynamics (warming).

The AR frequency increase manifests the intensifying hydrological cycle in the $\operatorname{Arctic}^{45-47}$, and could exert impacts beyond hydrology and the cryosphere. Combined with more frequent cyclones in the central Arctic and Chukchi Sea 48,49 , the resultant rainfall and snowfall are expected to undergo pronounced changes 50,51 , leading to a more stormy Arctic. These changes will increase the ecosystem fragility and human exposure to natural hazards in the Arctic as international ocean freight and fishing industries grow in the coming decades. Advancing our understanding of the changes in the synoptic weather systems such as ARs in a warming climate could lead to more credible projections of ecosystem changes and human adaptation to the growing impacts of global warming in the polar region.

Online content

Any methods, additional references, Nature Portfolio reporting summaries, source data, extended data, supplementary information, acknowledgements, peer review information; details of author contributions and competing interests; and statements of data and code availability are available at https://doi.org/10.1038/s41558-023-01599-3.

References

- Stroeve, J. C. et al. Trends in Arctic sea ice extent from CMIP5, CMIP3 and observations. Geophys. Res. Lett. 39. L16502 (2012).
- Bailey, H. et al. Arctic sea-ice loss fuels extreme European snowfall. Nat. Geosci. 14, 283–288 (2021).
- Cohen, J., Agel, L., Barlow, M., Garfinkel, C. I. & White, I. Linking Arctic variability and change with extreme winter weather in the United States. Science 373, 1116–1121 (2021).
- Zhang, P. et al. A stratospheric pathway linking a colder Siberia to Barents-Kara Sea sea ice loss. Sci. Adv. 4, eaat6025 (2018).
- Dalpadado, P. et al. Productivity in the Barents Sea—response to recent climate variability. PLoS ONE 9, e95273 (2014).
- Fossheim, M. et al. Recent warming leads to a rapid borealization of fish communities in the Arctic. Nat. Clim. Change 5, 673–677 (2015).
- Park, D.-S. R., Lee, S. & Feldstein, S. B. Attribution of the recent winter sea ice decline over the Atlantic sector of the Arctic Ocean. J. Clim. 28, 4027–4033 (2015).
- 8. Woods, C. & Caballero, R. The role of moist intrusions in winter Arctic warming and sea ice decline. *J. Clim.* **29**, 4473–4485 (2016).
- Hofsteenge, M. G., Graversen, R. G., Rydsaa, J. H. & Rey, Z. The impact of atmospheric Rossby waves and cyclones on the Arctic sea ice variability. *Clim. Dynam.* 59, 579–594 (2022).
- Petty, A. A., Holland, M. M., Bailey, D. A. & Kurtz, N. T. Warm Arctic, increased winter sea ice growth? *Geophys. Res. Lett.* 45, 12922–12930 (2018).
- Stroeve, J. & Notz, D. Changing state of Arctic sea ice across all seasons. Environ. Res. Lett. 13, 103001 (2018).
- Barton, B. I., Lenn, Y.-D. & Lique, C. Observed Atlantification of the Barents Sea causes the polar front to limit the expansion of winter sea ice. J. Phys. Oceanogr. 48, 1849–1866 (2018).
- Polyakov, I. V. et al. Borealization of the Arctic Ocean in response to anomalous advection from sub-Arctic seas. Front. Mar. Sci. 7, 491 (2020).
- 14. Skagseth, Ø. et al. Reduced efficiency of the Barents Sea cooling machine. *Nat. Clim. Change* **10**, 661–666 (2020).
- Tsubouchi, T. et al. Increased ocean heat transport into the Nordic Seas and Arctic Ocean over the period 1993–2016. Nat. Clim. Change 11, 21–26 (2021).
- Nash, D., Waliser, D., Guan, B., Ye, H. & Ralph, F. M. The role of atmospheric rivers in extratropical and polar hydroclimate. J. Geophys. Res. Atmos. 123, 6804–6821 (2018).
- Ralph, F. M. et al. Atmospheric rivers emerge as a global science and applications focus. *Bull. Am. Meteorol. Soc.* 98, 1969–1973 (2017).
- Zhu, Y. & Newell, R. E. A proposed algorithm for moisture fluxes from atmospheric rivers. Mon. Weather Rev. 126, 725–735 (1998).
- Newman, M., Kiladis, G. N., Weickmann, K. M., Ralph, F. M. & Sardeshmukh, P. D. Relative contributions of synoptic and low-frequency eddies to time-mean atmospheric moisture transport, including the role of atmospheric rivers. J. Clim. 25, 7341–7361 (2012).
- Lavers, D. A. & Villarini, G. The contribution of atmospheric rivers to precipitation in Europe and the United States. J. Hydrol. 522, 382–390 (2015).
- Chen, X., Leung, L. R., Wigmosta, M. & Richmond, M. Impact of atmospheric rivers on surface hydrological processes in western U.S. watersheds. J. Geophys. Res. Atmos. 124, 8896–8916 (2019).
- 22. Hegyi, B. M. & Taylor, P. C. The unprecedented 2016–2017 Arctic sea ice growth season: the crucial role of atmospheric rivers and longwave fluxes. *Geophys. Res. Lett.* **45**, 5204–5212 (2018).
- Gorodetskaya, I. V. et al. The role of atmospheric rivers in anomalous snow accumulation in East Antarctica. Geophys. Res. Lett. 41, 6199–6206 (2014).

- Mattingly, K. S., Mote, T. L. & Fettweis, X. Atmospheric river impacts on Greenland ice sheet surface mass balance.
 J. Geophys. Res. Atmos. 123, 8538–8560 (2018).
- 25. Wille, J. D. et al. West Antarctic surface melt triggered by atmospheric rivers. *Nat. Geosci.* **12**, 911–916 (2019).
- 26. Francis, D., Mattingly, K. S., Temimi, M., Massom, R. & Heil, P. On the crucial role of atmospheric rivers in the two major Weddell Polynya events in 1973 and 2017 in Antarctica. Sci. Adv. 6, eabc2695 (2020).
- Persson, P. O. G., Shupe, M. D., Perovich, D. & Solomon, A. Linking atmospheric synoptic transport, cloud phase, surface energy fluxes, and sea-ice growth: observations of midwinter SHEBA conditions. Clim. Dynam. 49, 1341–1364 (2017).
- 28. Doyle, S. H. et al. Amplified melt and flow of the Greenland ice sheet driven by late-summer cyclonic rainfall. *Nat. Geosci.* **8**, 647–653 (2015).
- 29. Ledley, T. S. Snow on sea ice: competing effects in shaping climate. *J. Geophys. Res. Atmos.* **96**, 17195–17208 (1991).
- Merkouriadi, I., Cheng, B., Hudson, S. R. & Granskog, M. A. Effect of frequent winter warming events (storms) and snow on sea-ice growth—a case from the Atlantic sector of the Arctic Ocean during the N-ICE2015 campaign. *Ann. Glaciol.* 61, 164–170 (2020).
- Wang, Z., Walsh, J., Szymborski, S. & Peng, M. Rapid Arctic sea ice loss on the synoptic time scale and related atmospheric circulation anomalies. J. Clim. 33, 1597–1617 (2020).
- Gao, Y., Lu, J. & Leung, L. R. Uncertainties in projecting future changes in atmospheric rivers and their impacts on heavy precipitation over Europe. J. Clim. 29, 6711–6726 (2016).
- 33. Ma, W., Chen, G. & Guan, B. Poleward shift of atmospheric rivers in the Southern Hemisphere in recent decades. *Geophys. Res. Lett.* **47**, e2020GL089934 (2020).
- 34. Payne, A. E. et al. Responses and impacts of atmospheric rivers to climate change. *Nat. Rev. Earth Environ.* **1**, 143–157 (2020).
- 35. Yang, W. & Magnusdottir, G. Springtime extreme moisture transport into the Arctic and its impact on sea ice concentration. *J. Geophys. Res. Atmos.* **122**, 5316–5329 (2017).
- Ding, Q. et al. Tropical forcing of the recent rapid Arctic warming in northeastern Canada and Greenland. *Nature* 509, 209–212 (2014).
- Meehl, G. A., Chung, C. T. Y., Arblaster, J. M., Holland, M. M. & Bitz,
 C. M. Tropical decadal variability and the rate of Arctic sea ice decrease. *Geophys. Res. Lett.* 45, 11,326–11,333 (2018).
- 38. Wu, Y., Lu, J., Ding, Q. & Liu, F. Linear response function reveals the most effective remote forcing in causing September Arctic sea ice melting in CESM. *Geophys. Res. Lett.* **48**, e2021GL094189 (2021).
- 39. Onarheim, I. H. & Årthun, M. Toward an ice-free Barents Sea. *Geophys. Res. Lett.* **44**, 8387–8395 (2017).
- Box, J. E. et al. Greenland ice sheet rainfall, heat and albedo feedback impacts from the mid-August 2021 atmospheric river. Geophys. Res. Lett. 49, e2021GL097356 (2022).
- 41. Fausto, R. S., van As, D., Box, J. E., Colgan, W. & Langen, P. L. Quantifying the surface energy fluxes in South Greenland during the 2012 high melt episodes using in-situ observations. *Front. Earth Sci.* **4**, 82 (2016).
- 42. Gettelman, A. et al. High climate sensitivity in the Community Earth System Model Version 2 (CESM2). *Geophys. Res. Lett.* **46**, 8329–8337 (2019).
- Luo, D. et al. Impact of Ural blocking on winter warm Arctic-cold Eurasian anomalies. Part I: blocking-induced amplification.
 J. Clim. 29, 3925–3947 (2016).
- Clark, J. P. & Lee, S. The role of the tropically excited Arctic warming mechanism on the warm Arctic cold continent surface air temperature trend pattern. *Geophys. Res. Lett.* 46, 8490–8499 (2019).

- Vihma, T. et al. The atmospheric role in the Arctic water cycle: a review on processes, past and future changes, and their impacts. J. Geophys. Res. Biogeosci. 121, 586–620 (2016).
- 46. Gimeno, L. et al. Atmospheric moisture transport and the decline in Arctic sea ice. *WIREs Clim. Change* **10**, e588 (2019).
- 47. Bintanja, R. et al. Strong future increases in Arctic precipitation variability linked to poleward moisture transport. Sci. Adv. 6, eaax6869 (2020).
- Zahn, M., Akperov, M., Rinke, A., Feser, F. & Mokhov, I. I. Trends of cyclone characteristics in the Arctic and their patterns from different reanalysis data. J. Geophys. Res. Atmos. 123, 2737–2751 (2018).
- Valkonen, E., Cassano, J. & Cassano, E. Arctic cyclones and their interactions with the declining sea ice: a recent climatology. J. Geophys. Res. Atmos. 126, e2020JD034366 (2021).
- Webster, M. A., Parker, C., Boisvert, L. & Kwok, R. The role of cyclone activity in snow accumulation on Arctic sea ice. *Nat. Commun.* 10, 5285 (2019).

- McCrystall, M. R., Stroeve, J., Serreze, M., Forbes, B. C. & Screen, J. A. New climate models reveal faster and larger increases in Arctic precipitation than previously projected. *Nat. Commun.* 12, 6765 (2021).
- 52. Swart, N. C., Fyfe, J. C., Gillett, N. & Marshall, G. J. Comparing trends in the southern annular mode and surface westerly jet. *J. Clim.* **28**, 8840–8859 (2015).

Publisher's note Springer Nature remains neutral with regard to jurisdictional claims in published maps and institutional affiliations.

Springer Nature or its licensor (e.g. a society or other partner) holds exclusive rights to this article under a publishing agreement with the author(s) or other rightsholder(s); author self-archiving of the accepted manuscript version of this article is solely governed by the terms of such publishing agreement and applicable law.

@ The Author(s), under exclusive licence to Springer Nature Limited 2023

Methods

Observational datasets

Three reanalysis datasets were employed in this study: ERA5⁵³ for 1979–2021 at a resolution of 0.5° \times 0.5°, National Aeronautics and Space Administration (NASA) Modern-Era Retrospective analysis for Research and Applications, version 2 (MERRA2)⁵⁴ for 1980–2021 at 0.625° \times 0.5° and JRA55⁵⁵ for 1979–2021 at 1.5° \times 1.5°. We focused on the long-term changes during the sea-ice seasonal recovery months NDJ, and thus there were 42 NDJ in ERA5 and JRA55 and 41 NDJ in MERRA2 that were analysed. Daily variables were used, but the results were robust using 6-h data (see Supplementary Fig. 1a versus Fig. 2a). See Supplementary Text 4 for quality and validation of reanalysis data.

The sea-ice data were obtained from the NOAA/National Snow and Ice Data Center (NSIDC) climate data record of satellite passive microwave SIC, version 4 (ref. 56). Both daily and monthly SIC estimates for 1979–2021 from the NASA Bootstrap algorithm on a 25 km × 25 km grid were used. Note that satellite observations were missing during the 1987-1988 winter. The sea-ice cover edge was defined as the 15% contour of SIC by convention. The region between the climatological ice edges on 31 October and 1 January (the red and blue lines in Fig. 1a,b, Fig. 3 and Supplementary Fig. 4) are referred to as the marginal ice zone. Sea-ice coverage can be measured in terms of both ice area and ice extent (see NSIDC terminology: https://nsidc.org/learn/cryosphere-glossary/i). Sea-ice extent measures the ocean region surrounded by the sea-ice cover edge line. SIA at each grid cell was calculated as SIC multiplied by the cell area (that is, the area of the portion of the cell covered by ice). For example, for a grid cell with SIC of 50%, the whole grid cell was treated as ice-covered (SIC > 15%) in determining sea-ice extent, while only 50% of the grid cell was counted in SIA. There was almost no difference between sea-ice exent and SIA in terms of long-term change or large scales. We used SIA in this study because SIA represented the exact change in SIC and thus was appropriate to reflect the impact of ARs at the synoptic temporal and spatial scales. The NDJ SIA growth in Fig. 4 was defined as the cumulative sum of daily anomalies of SIA tendency in NDJ. The SIA tendency on day i was defined as $(SIAi+1-SIA_{i-1})/2$, where i denotes the day number from 1 November to 31 January. The daily anomaly was the deviation from the daily climatology of the whole study period of each dataset smoothed with a 15-day moving average window. SIA growth associated with (without) AR was the cumulated sum of SIA tendency with (without) AR occurrence. We focused on ice coverage because of the distinct surface energy balance and air-sea interaction with and without ice cover on the sea surface.

Model experiments and interpretation

This study involved a series of model ensemble experiments conducted by the Climate Variability and Change Working Group at the National Center for Atmospheric Research using the state-of-the-art global climate model CESM2. First, the 50-member CESM2 Large Ensemble (LENS2)⁵⁷ outputs were employed. LENS2 covered the period from 1850 to 2100 under Coupled Model Intercomparison Project Phase 6 (CMIP6) historical (before 2014) and SSP370 (from 2015) future radiative forcing scenarios. Each ensemble member was forced in an identical way, except for the initial conditions. The LENS2 ensemble can be regarded as an expansion set of the CESM2 simulations in the CMIP6 archive. The results in LENS2 were therefore generally similar to the CESM2 simulations in CMIP6, which we have confirmed. Second, we examined a ten-member atmosphere-only simulation from CAM6, the atmospheric component of CESM2, forced by the same external forcing as LENS2 and prescribed time-varying SST from NOAA Extended Reconstruction Sea Surface Temperature Version 5 (ERSSTv5) and Hadley Centre sea ice (HadISST1) from 1880 to 2019, named Global Ocean Global Atmosphere. This set of simulations was called GOGA2 to differentiate it from a similar set of simulations produced by CAM5/CESM1. Third, we analysed a ten-member pacemaker historical experiment with CESM2 in which the SSTa in the tropical Pacific were nudged to observations (ERSSTv5). The nudging mask covered the tropical Pacific from the American coast to the western Pacific between 20° S-20° N, with the form of a wedge shape toward the Maritime Continent to the west of the dateline, and a 5° buffer region where the strength of the relaxation was linearly reduced. In each pacemaker run, the model-simulated temporal SSTa was replaced with the observed evolution of SSTa (that is, the tropical Pacific SSTa was the pacemaker), with the rest of the model's coupled climate system free to evolve. Since only the anomalies were nudged, the nudging did not alter the mean state of the model. In the period between the 1980s and 2010s, there was a decadal cooling trend in the tropical Pacific (that is, a La Niña-like change), known as the phase transition of the Inter-decadal Pacific Oscillation or Pacific Decadal Oscillation, the leading mode of internal variability at the decadal timescale featuring SST variability in the Pacific Ocean (see https://www.cesm.ucar.edu/working_groups/ CVC/simulations/cesm2-pacific pacemaker.html for the nudging mask area and the details of the Pacific Pacemaker experiments). This CESM2 Pacific Pacemaker ensemble was called PAC2 in this study.

The daily and monthly outputs were available at the same resolution of $0.9^{\circ} \times 1.25^{\circ}$. We only analysed the outputs for 1979–2014 in which all experiments were forced by the historical forcing to facilitate a comparison to the observations, that is, 35 NDJ in each member for analysis.

As the three experiments (GOGA2, LENS2 and PAC2) shared the same radiative forcing and used the same atmospheric model, the differences among them lay in the surface boundary conditions for the atmosphere: prescribed observed SST (GOGA2), coupled ocean-atmosphere except for the tropical Pacific SST that is constrained by the observed Inter-decadal Pacific Oscillation evolution (PAC2) and fully coupled ocean-atmosphere (LENS2). With these experimental set-ups, the climate evolution in GOGA2 was most comparable to observations, followed by PAC2, while LENS2 was free to evolve subject only to external forcing.

We interpreted the model results following the well-established approach in the climate modelling community (for example, refs. 58-60). The observed climate reflected the combination of the radiatively forced response and a specific realization of the natural variability. Because the latter was random, we would not expect an individual member of the free-running model ensembles to closely resemble the observations. Although free-running models cannot perfectly reproduce the exact phase of the observed natural variability, model ensembles can be used to separate the influences of external forcing and internal variability. The influence of anthropogenic forcing can be estimated by the ensemble mean of LENS2 because each member of the ensemble is influenced by the same external forcing. The internal variability was largely suppressed by averaging across the individual ensemble members, which featured different realizations of the random natural variability. In other words, the spread among the ensemble members in LENS2 represented the effects of random internal variability. With the tropical Pacific SSTa nudged to the observations, the PAC2 ensemble spread represented internal variability associated with regions outside the tropical Pacific and with internal atmospheric dynamics. Its ensemble mean reflected the combination of the anthropogenically forced responses and the model's responses to the observed tropical Pacific SST variability. As PAC2 and LENS2 shared the same model configurations, their forced responses should in principle be the same, and therefore the forced response in both LENS2 and PAC2 can be represented by the ensemble mean of LENS2. Then, the role of the tropical Pacific SST variability, called tropical Pacific influence, can be isolated by subtracting the LENS2 ensemble mean from the PAC2 mean⁵⁸⁻⁶⁰. The tropical Pacific influence is an estimate of the variability in the climate system that is associated with tropical Pacific SSTs. Holland et al. 58 concluded that this approach allows us to consistently compare the magnitude of climate responses (for example, Arctic AR changes) to anthropogenic forcing and tropical Pacific variability. The significant difference between the PAC2 and LENS2 mean AR trends in northern ABK and inland Eurasia (Fig. 5d) suggests that the Pacific variability played a detectable role in the high-latitude AR trend during recent decades.

There are caveats in understanding the influence of tropical Pacific variability based on the model experiments. First, the estimate of the tropical influence assumes that the responses to tropical Pacific variability and external forcings are independent. Indeed, they are largely linearly separable for all practical purposes (for example, refs. 61-63), although this assumption may not strictly hold. In any case, it is difficult to completely separate the external and tropical signals. Thus, the linear assumption neglects the impact of external forcing on tropical Pacific variability 58. Second, it is possible that the forced response in LENS2 and PAC2 may not be the same. Nevertheless, many previous studies have shown that the above approach practically and realistically delineates the response to tropical Pacific variability (for example, refs. 58-60).

Third, some biases in model physics may affect sea-ice simulation and the impact of ARs on sea ice in CESM2. Over the Arctic, the CESM2 configuration has thinner liquid clouds and a smaller cloud fraction due to underestimated aerosols. This leads to increased shortwave radiation received by sea ice in melt season and thus an insufficient late summer Arctic sea-ice cover, while the sea-ice coverage bias is relatively small in winter (for example, refs. 64,65). The sea-ice bias could produce a fasterice growth in early winter, debasing the significance of the melting effect of ARs on sea ice in CESM2 simulations, as we can see in Fig. 4. In addition, smaller cloud fractions may also reduce the contribution of cloud to DLW. Climate models do not consider the heat conduction from rainfall to sea ice. On the other hand, the winter ice thickness in CESM2 is biased thin in historical simulations⁶⁶, which could enhance the melting effect of ARs. That is to say, biases in CESM2 physics may partly cancel each other to simulate the impact of ARs on sea ice. These limitations could explain the weaker melting effect of ARs simulated in PAC2 than observation (Fig. 4). Furthermore, given that the Gulf Stream warming in CESM2 lies towards the higher end of CMIP6 models⁶⁷, the underestimation of the winter SIC decline in the Barents-Kara Seas in recent decades in CESM2 (see ref. ⁶⁷ or Supplementary Fig. 4) may be attributable to the underestimation of atmospheric influences such as the melting effect of weaker ARs in CESM2. Nevertheless, given that the ensembles employed in the current study are based on the same model, the model bias may be cancelled when one ensemble is subtracted from another and thus may not affect the understanding of the tropical Pacific influence obtained from PAC2 minus LENS2.

AR detection and analysis methods

We employed an IVT-based (Supplementary Text 1) AR detection algorithm originally developed in ref. 68 and slightly optimized it for the Arctic, following ref. 24. The algorithm by ref. 68 is recommended by the Atmospheric River Tracking Method Intercomparison Project (ARTMIP), especially for research on ARs in polar latitudes and inland regions⁶⁹. ARTMIP noted that this algorithm is one of the methods that facilitates the attribution of impacts within the AR footprint⁶⁹. In fact, all ARTMIP global algorithms tend to agree remarkably well on the AR footprints⁷⁰. In the algorithm used in this study, the monthly dependent 85th percentile of the IVT magnitude at each grid cell, or 100 kg m⁻¹ s⁻¹, whichever was greater, was used as the intensity threshold to identify contiguous regions with elevated IVT. In practice, the 85th percentile IVT was the threshold used in the mid-latitudes, which is the same as many other algorithms⁶⁹, while 100 kg m⁻¹ s⁻¹ was the actual threshold used in the Arctic region because of the low IVT due to low air temperature. We also checked the ARs with relative thresholds in the Arctic, and the results were not sensitive to the choice of thresholds (Supplementary Text 2 and Supplementary Fig. 1d-f). Potential ARs were then filtered by applying size, length, length-to-width ratio, coherence, the meridional component of mean IVT and mean transport direction criteria. We followed ref. 24 to change the length criterion from 2,000 km to 1,500 km, considering that the ARs reaching the Arctic are usually at the end of their lifecycle and their size is decreased. In fact, the results were not sensitive to the change in length criterion. These requirements ensured that the identified characteristics were long, narrow, coherent belts of poleward moisture transport in (and connecting) the mid-latitudes and polar regions, thus bearing the features of ARs. See refs. ^{24,68} for additional details of the AR detection algorithm.

A scaling method³³ was employed to separate the thermodynamic effect and the dynamical effect in the AR frequency trend. We created a hypothetical scenario of daily IVT with dynamic effect only by applying a scaling coefficient to specific humidity, given that the moisture changes were expected to scale in line with the Clausius-Clapeyron relationship. Specifically, the specific humidity was scaled by a factor q_c/q_s , where q_c is the climatological specific humidity in NDJ at the level and grid to which this factor applies and q_s is the seasonal mean specific humidity at the same grid for the given NDJ. By scaling the data this way, the year-to-year change in specific humidity was removed. Then, the IVT calculated with the scaled moisture field and the same threshold were used as input to the AR detection algorithm. As a result, the effect of the background moisture interannual variability on AR variability was suppressed, allowing the AR trend due to the dynamic effect to be estimated. The two components were found to be largely linearly additive using the same method⁷¹. Therefore, we calculated the thermodynamic effect as the difference between the total trend and the dynamic effect.

Variable (DLW, rainfall, snowfall, SIC and so on) anomalies associated with ARs at a grid were detected if an AR appeared at this grid. The climatology or reference state refers to the mean of the whole study period of each dataset smoothed with a 15-day moving average window. For the AR-related trends in variables (DLW, CRE, rainfall and snowfall) shown in Fig. 3, Supplementary Fig. 2b and Extended Data Figs. 2 and 3, we first integrated the variable associated with ARs in NDJ over time (that is, the total/cumulated amount of these fluxes related to ARs) and then calculated the trends. The contribution of CRE to DLW was the difference between surface DLW and clear sky DLW. The impact of ice drifting related to AR wind on ABK SIA was much smaller than that of the melting effect of ARs (Supplementary Text 5) and thus was not involved in this study.

Linear projection was used to determine the amount of enhancement of AR melting effect due to AR frequency increase. We first calculated the melting effect on SIA corresponding to 1% AR frequency (-0.92 day) occurrence based on the SIA growth with AR (red line in Fig. 4) and AR frequency (Fig. 2b) in NDJ, which on average was a reduction of $-8.8 \pm 0.6 \times 10^4 \, \mathrm{km^2}$ in the ABK SIA in NDJ in the observation. Uncertainty was measured by the standard error computed from interannual time series. Then we estimated the enhancement of the melting effect due to AR frequency increase by projecting the SIA reduction corresponding to 1% AR frequency to the actual trend in AR frequency (Fig. 2b) and finally inferred its contribution (-34 \pm 2%) to the SIA decline in the ABK in NDJ (red line in Fig. 2b). The estimation was 30 \pm 5% in PAC2 due to a weaker melting effect simulated in CESM2. The uncertainty in PAC2 was the standard error across ensemble members.

Statistics

Two-sided Student's t-tests were used in the significance test for the linear trend in observations. A two-sided 1,000 bootstrap resampling with replacement was used in the significance tests for the composite analysis and the trends in model ensembles. In Fig. 5e, following ref. 52 , the uncertainty in the mean trend of an ensemble is represented by the 95% confidence interval, which is given by $\bar{b} \pm \frac{C_b}{\sqrt{n}}$, where \bar{b} is the ensemble mean of the trends calculated from individual ensemble members, n is the ensemble size, c is the 97.5th percentile of the Student's t distribution with t 1 degrees of freedom and t 2 is an estimate of the inter-member standard deviation of the trends. We calculated this 95% confidence interval for the ensemble mean of GOGA2, LENS2 and PAC2, shown as the vertical colour bars in Fig. 5e. The pattern correlation coefficient was employed to measure the pattern similarity with latitudinal weights considered.

Data availability

ERA5, MERRA2 and JRA55 reanalysis data are available at https://cds.climate.copernicus.eu/#!/home, https://gmao.gsfc.nasa.gov/

reanalysis/MERRA-2/data_access/ and https://jra.kishou.go.jp/JRA-55/index_en.html. NSIDC SIC data are available from https://nsidc.org/data/G02202. The CESM2 simulations used in this study are available at: CESM2 Large Ensemble Community Project (https://www.cesm.ucar.edu/community-projects/lens2/data-sets), CESM2 Pacific Pacemaker Ensemble⁷² (https://www.earthsystemgrid.org/dataset/ucar.cgd.cesm2.pacific.pacemaker.html) and CAM6 Prescribed SST AMIP ensembles (https://www.cesm.ucar.edu/working-groups/climate/simulations/cam6-prescribed-sst). CESM2 pre-industrial outputs are available from the Coupled Model Intercomparison Project Phase 6 archive at https://pcmdi.llnl.gov/CMIP6/. See the Supplementary Information for the data information of the datasets only used in supplementary.

Code availability

The code⁷³ for the AR detection method used in this study is available via the UCLA Dataverse at https://doi.org/10.25346/S6/SJGRKY. The results, data and codes⁷⁴ used to produce Figs. 1–6 are available via figshare at https://doi.org/10.6084/m9.figshare.21405051.v2.

References

- CESM2 Pacific Pacemaker Ensemble (NCAR, 2022); https://doi. org/10.26024/gtrs-tf57
- Guan, B. Tracking atmospheric rivers globally as elongated targets (tARget), version 1. *UCLA Dataverse* https://doi. org/10.25346/S6/SJGRKY (2021).
- Zhang, P. & Chen, G. Replication data for Zhang et al. 2022 Arctic ARs. figshare https://doi.org/10.6084/m9.figshare.21405051.v2 (2022).
- Hersbach, H. et al. The ERA5 global reanalysis. Q. J. R. Meteorol. Soc. 146, 1999–2049 (2020).
- Gelaro, R. et al. The Modern-Era Retrospective analysis for Research and Applications, Version 2 (MERRA-2). J. Clim. 30, 5419–5454 (2017).
- Kobayashi, S. et al. The JRA-55 reanalysis: general specifications and basic characteristics. J. Meteorol. Soc. Jpn Ser. II 93, 5–48 (2015).
- Meier, W. N., Fetterer, F., Windnagel, A. K. & Stewart, J. S. NOAA/ NSIDC Climate Data Record of Passive Microwave Sea Ice Concentration, Version 4 (NSIDC, 2021); https://doi.org/10.7265/ efmz-2t65
- 60. Rodgers, K. B. et al. Ubiquity of human-induced changes in climate variability. *Earth Syst. Dynam.* **12**, 1393–1411 (2021).
- Holland, P. R., Bracegirdle, T. J., Dutrieux, P., Jenkins, A. & Steig, E. J. West Antarctic ice loss influenced by internal climate variability and anthropogenic forcing. *Nat. Geosci.* 12, 718–724 (2019).
- 62. Schneider, D. P. & Deser, C. Tropically driven and externally forced patterns of Antarctic sea ice change: reconciling observed and modeled trends. *Clim. Dynam.* **50**, 4599–4618 (2018).
- 63. Yang, D. et al. Role of tropical variability in driving decadal shifts in the Southern Hemisphere summertime eddy-driven jet. *J. Clim.* **33**, 5445–5463 (2020).
- Ting, M., Kushnir, Y., Seager, R. & Li, C. Forced and internal twentieth-century SST trends in the North Atlantic. J. Clim. 22, 1469–1481 (2009).
- DelSole, T., Tippett, M. K. & Shukla, J. A significant component of unforced multidecadal variability in the recent acceleration of global warming. J. Clim. 24, 909–926 (2011).
- Lu, J., Hu, A. & Zeng, Z. On the possible interaction between internal climate variability and forced climate change. Geophys. Res. Lett. 41, 2962–2970 (2014).
- DuVivier, A. K. et al. Arctic and Antarctic sea ice mean state in the Community Earth System Model Version 2 and the influence of atmospheric chemistry. J. Geophys. Res. Oceans 125, e2019JC015934 (2020).

- 68. Kay, J. E. et al. Less surface sea ice melt in the CESM2 improves Arctic sea ice simulation with minimal non-polar climate impacts. *J. Adv. Model. Earth Syst.* **14**, e2021MS002679 (2022).
- DeRepentigny, P., Jahn, A., Holland, M. M. & Smith, A. Arctic sea ice in two configurations of the CESM2 during the 20th and 21st centuries. J. Geophys. Res. Oceans 125, e2020JC016133 (2020).
- 70. Yamagami, Y., Watanabe, M., Mori, M. & Ono, J. Barents-Kara sea-ice decline attributed to surface warming in the Gulf Stream. *Nat. Commun.* **13**, 3767 (2022).
- 71. Guan, B. & Waliser, D. E. Detection of atmospheric rivers: evaluation and application of an algorithm for global studies. *J. Geophys. Res.* **120**, 12514–12535 (2015).
- 72. Rutz, J. J. et al. The Atmospheric River Tracking Method Intercomparison Project (ARTMIP): quantifying uncertainties in atmospheric river climatology. *J. Geophys. Res. Atmos.* **124**, 13777–13802 (2019).
- 73. Lora, J. M., Shields, C. A. & Rutz, J. J. Consensus and disagreement in atmospheric river detection: ARTMIP global catalogues. *Geophys. Res. Lett.* **47**, e2020GL089302 (2020).
- 74. Zhang, P., Chen, G., Ma, W., Ming, Y. & Wu, Z. Robust atmospheric river response to global warming in idealized and comprehensive climate models. *J. Clim.* **34**, 7717–7734 (2021).

Acknowledgements

We thank J. Lu at PNNL and S. Lee and S. B. Feldstein at PSU for helpful discussions. We would like to acknowledge the NCAR's CESM project which is supported by NSF and CESM's CVCWG and the Computational Information Systems Laboratory NCAR Community Computing resources (doi: 10.5065/D6RX99HX) for providing the CESM simulations used in this study and thank A. Phillips and I. R. Simpson at NCAR for helpful information on these model outputs. P.Z. was supported by PSU. NSF grant number AGS-1832842 and NASA grant number 80NSSC21K1522 were awarded to G.C. NASA award number 80NSSC20K1254 and NSF award number OPP-1825858 were awarded to M.T. L.R.L was supported by the Office of Science, US Department of Energy Biological and Environmental Research as part of the Regional and Global Model Analysis programme area. B.G. was supported by NASA and the California Department of Water Resources. NASA grant number 21-OSST21-0006 was awarded to L.L. Pacific Northwest National Laboratory is operated for the Department of Energy by Battelle Memorial Institute under contract no. DE-ACO5-76RL01830.

Author contributions

P.Z. conceived the study, analysed the data and wrote the initial draft of the paper. G.C., M.T. and L.R.L. provided feedback on analysis and contributed to constructive revisions. All authors contributed to editing and revisions.

Competing interests

The authors declare no competing interests.

Additional information

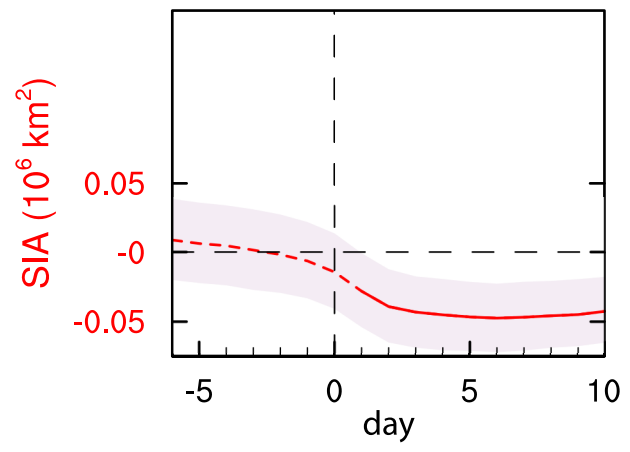
Extended data is available for this paper at https://doi.org/10.1038/s41558-023-01599-3.

Supplementary information The online version contains supplementary material available at https://doi.org/10.1038/s41558-023-01599-3.

 $\begin{tabular}{ll} \textbf{Correspondence and requests for materials} should be addressed to Pengfei Zhang. \end{tabular}$

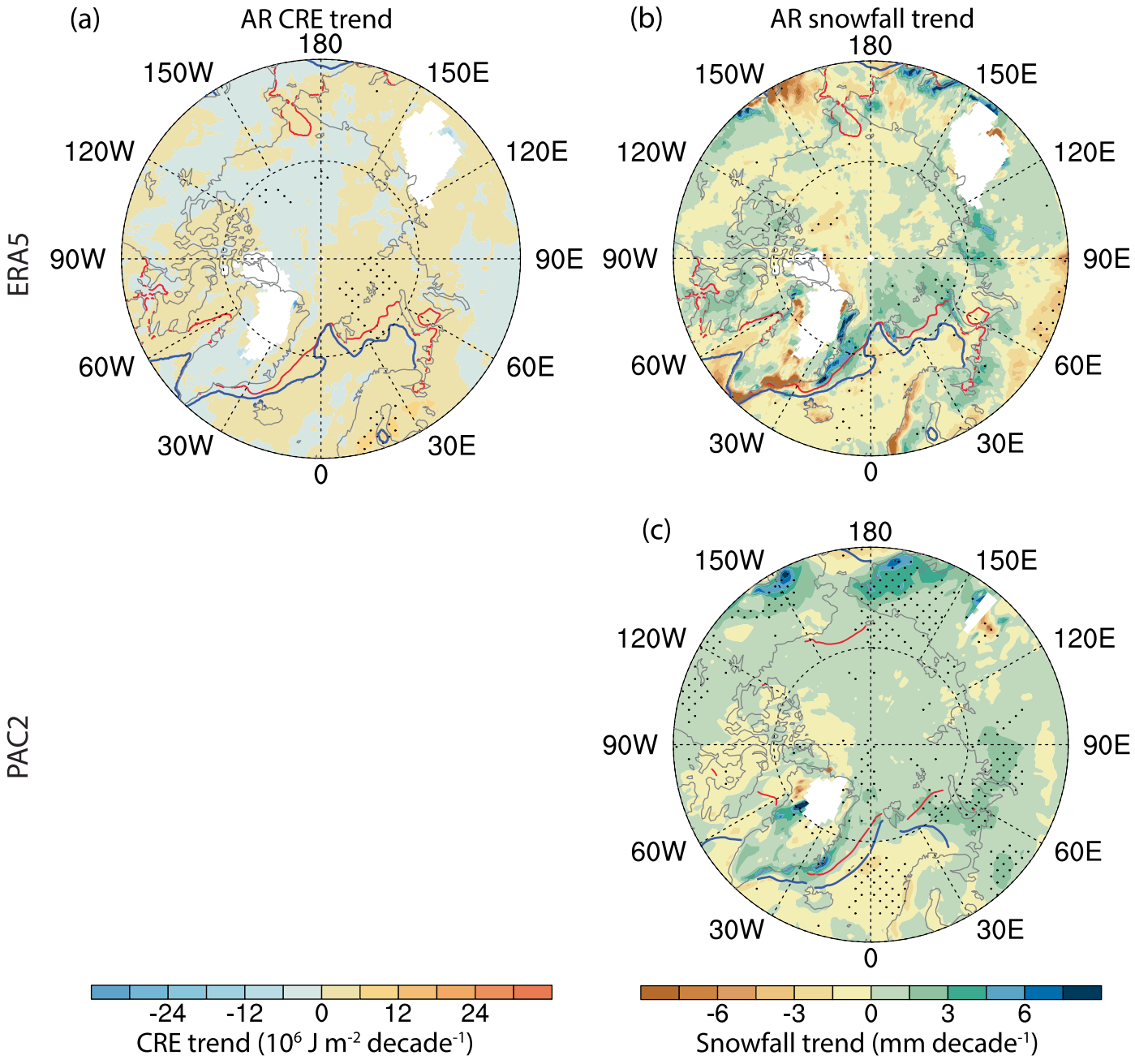
Peer review information *Nature Climate Change* thanks Rune Graversen, Kyle Mattingly and the other, anonymous, reviewer(s) for their contribution to the peer review of this work.

Reprints and permissions information is available at www.nature.com/reprints.



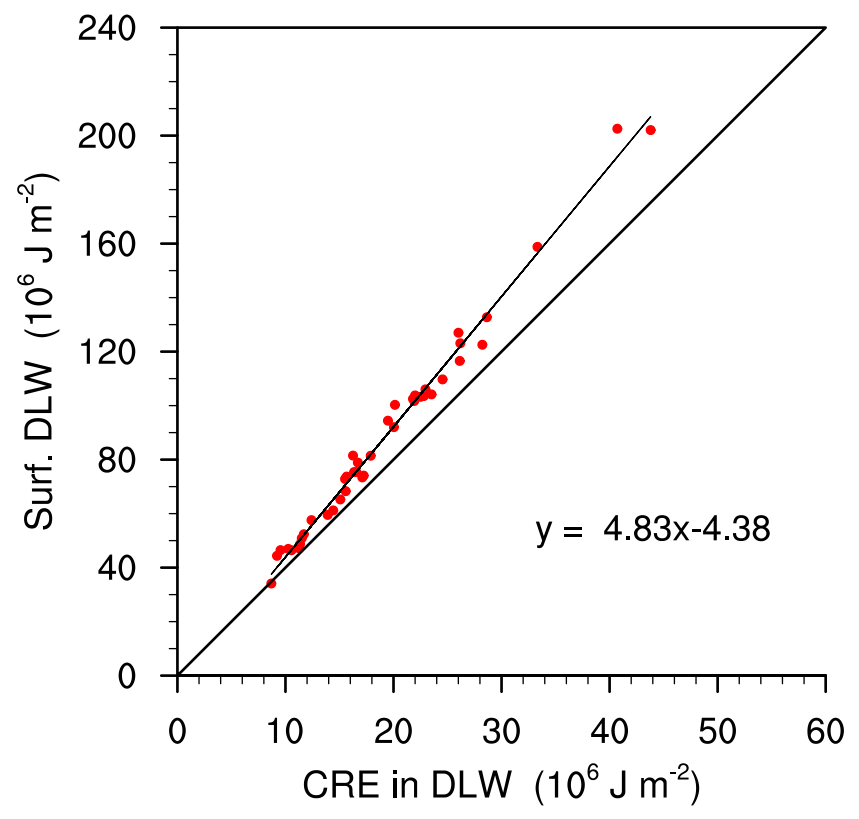
Extended Data Fig. 1 | ABK SIA anomalies when ARs make landfalling on the ice cover in CESM2 pre-industrial simulation. Same as the composite SIA anomalies in Fig. 1c but for a 40-year segment (1160-1199) from CESM2 pre-industrial simulation. There is no significant background trend in the Arctic in these 40 years. The same AR detection procedure is conducted for these 40

years using daily data. The color shadings denote the 2.5-97.5% intervals of the anomalies, and the solid segments denote the significant anomalies based on 1000 bootstrap samples. The SIA anomalies show a significant retreat following ARs reaching the ice edge, supporting the results in observations (Fig. 1c).

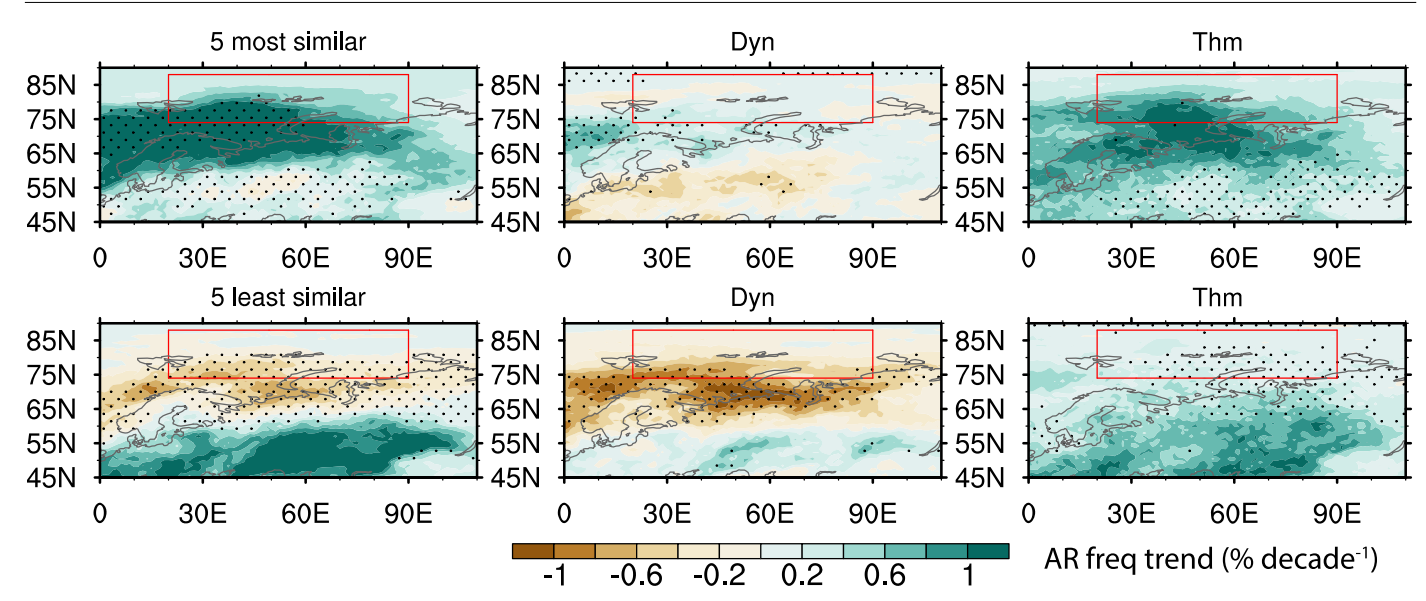


Extended Data Fig. 2 | AR-induced trends in cloud radiative effect in cumulated DLW (left) and snowfall (right) in NDJ in ERA5 (a,b) and the model ensemble from PAC2 (c). See Method for the calculation details of the total amounts of the flux variables associated with ARs in NDJ. The cloud radiative effect of DLW is expressed as the difference between DLW and clear sky DLW. The

cloud radiative effect of longwave radiation in PAC2 is missing due to no clear sky DLW output in PAC2. Dots denote trends that are statistically significant at the 0.05 level according to the t-test for ERA5 and the 1000 bootstrap samples for PAC2.



Extended Data Fig. 3 | Proportional contribution of cloud radiative effect to the cumulated surface DLW related to ARs in NDJ for 1979-2021 in ERA5. The linear fit is shown as the black line and the equation.



Extended Data Fig. 4 | **AR frequency trend in selected individual members in LENS2.** The left column shows the mean AR frequency trend in 5 LENS2 members who are most (least) similar to GOGA2 in the area of $(0^{\circ}-110^{\circ}E, 45^{\circ}-90^{\circ}N)$. Here, we regard the AR trend pattern in GOGA2 as the reference pattern considering the system consistency. The results are similar for using PAC2 as the reference pattern. The middle and right columns are the contributions of dynamic and

thermodynamic effects, similar to that in Fig. 6. The dots indicate the AR changes are significantly different from the other 45 members in LENS2 at the 0.05 level based on 1000 bootstrap samples. The results are similar in the composites of the LENS2 sub-ensembles with the largest (smallest) trends in ABK, which we have confirmed.